Extreme Mechanics Letters 56 (2022) 101883

Contents lists available at ScienceDirect

Extreme Mechanics Letters

journal homepage: www.elsevier.com/locate/eml

Fracture resistance of 3D nano-architected lattice materials

Marco Maurizi [a,*], Bryce W. Edwards [b], Chao Gao [a], Julia R. Greer [b], Filippo Berto [a]

[a] NTNU - Norwegian University of Science and Technology–Department of Mechanical and Industrial Engineering, 7491 Trondheim, Norway
[b] Division of Engineering and Applied Science, California Institute of Technology, Pasadena, CA 91125, USA

ARTICLE INFO

Article history:
Received 16 May 2022
Received in revised form 19 July 2022
Accepted 15 August 2022
Available online 19 August 2022

Keywords:
Architected materials
Lattices
Fracture toughness
Crack propagation

ABSTRACT

Exploiting small scale material effects and structural topology, nano-architected lattices represent a recent novel class of mechanical metamaterials, which exhibit unprecedented combination of mechanical properties. Together with scarce resistance to fracture and catastrophic failure, understanding of the fracture characteristics and properties of 3D nano-architected lattices still represents a limiting factor for the design and realization of future engineering applications. Here, using a combination of in-situ tensile fracture experiments and finite element simulations, we first show the possibility to reach stable crack growth in nano-architected materials harnessing only the intrinsic plastic toughening mechanism. Exploring the effect of lattice topology on the fracture properties, we then demonstrate similar performance between the octet and 3D kagome architecture (along one direction). Based on the experimental and numerical results, a power-scaling law of normalized crack initiation toughness with relative density $\overline{\rho}$ (i.e., fraction of material per unit volume) $K_{IC}/\sigma_y \sqrt{L} \propto \overline{\rho}^{1.11}$, $\overline{\rho}^{1.17-1.27}$ is exhibited by the octet and 3D kagome topology, respectively, given the yield strength σ_y and the unit cell size L. Owing to the combination of the parent material's size effect and plasticity (3D-printed photo-resist polymer), the fracture initiation toughness (considering $\sigma_y = 27$ MPa) of our octet nano-architected lattices is ~ 8 times that of previously realized macroscopic octet titanium structures. After crack initiation, the two architectures manifest rising (in average $\sim$ 18%) fracture resistance curves (i.e., R-curves), without catastrophic failure. In addition, we find that the fracture toughness of architected lattices, measured by means of compact tension specimens, seems not to be dependent on the sample's thickness, forcing to re-think the plain strain toughness definition for this class of materials. Our results uncover the basic fracture characteristics of 3D architected materials exhibiting stable crack growth, providing insights for the design of light-weight, tough materials, with implications for future macro-scaled structural applications.

1. Introduction

Optimized arrangements of matter in the form of lattices, from atomic configuration in solid materials (i.e., crystalline structure) to biological systems, such as glass sponges (i.e., *Euplectella* [1]) and human bones (i.e., *cancelleous* bone [2]), seem to be very common in nature. Governed by the principle of minimum energy, natural materials organize themselves in hierarchical structures from nano- to macro-scale, efficiently exploiting the scarce available resources whilst achieving high mechanical performance [3–6]. Arranging material into ordered lattice structures down to the nano-scale allows indeed to exploit intrinsic material size effects, such as the increase of strength [7] and the emergence of flaw insensitivity [8]. With the possibility to 3D print small structures, several micro- and nano-architected materials have been recently realized [9–13], giving rise to a new era of high-performing mechanical metamaterials [14–17], from ultra-light and ultra-stiff micro-lattices [18], glassy carbon nanolattices approaching the theoretical strength [19], to supersonic impact resilient nano-architected materials [20].

Although mechanical robustness of materials is surely linked to high stiffness and strength, fracture behavior is what often limits the adoption of lightweight yet strong materials in engineering applications. The first work investigating the fracture toughness of brittle foams dates back to the 1984 [21]. Since then, numerous studies have been mainly focused on fracture of 2D brittle lattices [22–24], completely disregarding the investigation of the overall crack growth resistance (i.e., resistance to fracture during crack propagation) of 3D lattices. Evidence has been provided for the possibility to computationally predict the fracture toughness and crack growth resistance of 2D elasto-plastic lattice materials [25–27], and 3D macro-lattices [28,29]. Although a few studies have recently attempted to shed light on the fracture properties of brittle nano-architected lattices [30,31], the ability to accommodate fracture, leading to stable crack growth (i.e., avoiding catastrophic failure), has remained largely unexplored.

* Corresponding author.
E-mail address: marco.maurizi@ntnu.no (M. Maurizi).

https://doi.org/10.1016/j.eml.2022.101883

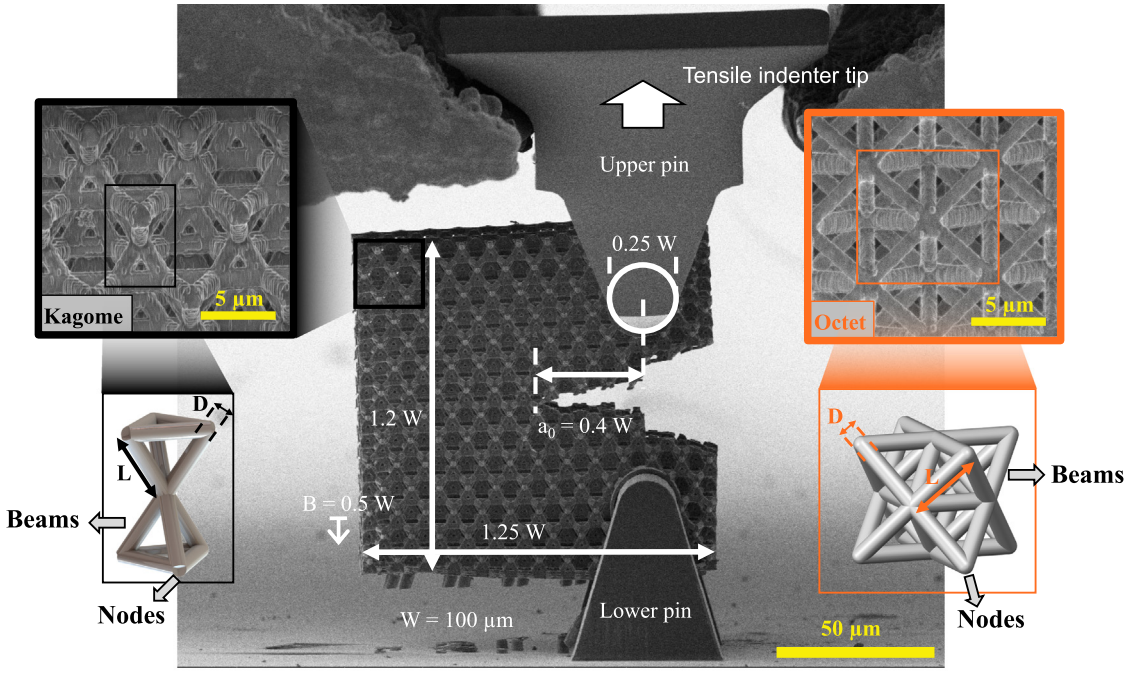

Fig. 1. Overview of in-situ fracture experiments on nano-architected CT specimens and investigated lattice topologies. Specimen design is based on ASTM standard for measurement of fracture toughness in traditional materials [33].

We performed a systematic study on the fracture behavior of 3D nano-architected lattices, providing evidence of peculiar fracture characteristics, highly dependent on the lattice topology. As the architecture of biological structural materials represents the main leverage to attain high mechanical performance given the parent material, we combined experimental and computational analyses to explore the effects of lattice topology on the fracture initiation and crack growth toughness of 3D nano-architected materials. We fabricated, tested, simulated and analyzed compact tension (CT) nano-architected specimens under quasi-static tensile loading, reaching stable crack growth conditions up to complete failure. We first unveiled the fracture resistance performance of the octet compared to the 3D kagome topology (along one direction, see inset in 1). Second, we demonstrated that our octet nano-architected lattices are ∼8 times tougher than macroscopic octet titanium structures. We also found that the ordinary decrease of fracture toughness from plane stress to plane strain conditions (i.e., increasing the specimen's thickness) does not hold for architected lattice materials, as also recently suggested [32]. Finally, we uncovered the detrimental effects of imperfections on the fracture properties of these materials, exhibiting a topology-dependent fracture toughness drop of ∼15%–21% and 7%–18% at crack initiation and during crack propagation, respectively. These results suggest that the influence of topology on the fracture resistance of 3D nano-architected lattice materials could be exploited to design stronger lightweight yet tougher novel metamaterials, in which the typical decrease of performance at low relative densities (by a power-scaling law $\propto \overline{\rho}^{\beta}$) may be counterbalanced by intelligently design ad hoc topologies. Besides, the invariance of the fracture toughness with different states of stress around the crack tip may pave the way for future up-scaled structural applications of nano-architected materials preserving high mechanical performance.

2. Results and discussion

To understand the fracture resistance of these materials during crack initiation and propagation, we fabricated CT nano-architected specimens out of IP-Dip photoresist (cross-linked polymer) using two-photon lithography (Fig. 1). Two monolithic pins (i.e., loading structures) were realized to allow the loading by the tension grips (see Methods for details). The CT specimen design comes from the standard test method for measurement of fracture toughness [33] of classic materials. We chose the CT design as the most suitable testing configuration, in contrast to other designs such as the single edge notched specimen, due to mainly the large deflections encountered (see Supplementary Video 1), a direct consequence of the ductile behavior of the parent material. This latter was primarily selected to allow the investigation of quasi-static crack growth under large deformations. Besides, aiming at studying the lattices' inherent fracture resistance, we focused only on the intrinsic toughening mechanisms, such as the plasticity effect ahead the crack front, generated by the ductile parent material (Fig. 2; see also Supplementary Section S4 and Supplementary Fig. 12). To explore the effect of lattice topology, we selected two different architectures, the octet and the 3D kagome (Fig. 1), primarily motivated by the high fracture performance of the 2D corresponding versions (i.e., triangular and 2D kagome, Refs. [24,26]). The octet architecture can be considered as a stretching-dominated topology (i.e., its beams are mainly under tension or compression); the 3D kagome falls between bending- (i.e., beams subjected to bending) and stretching-dominated topologies [34]. In the attempt to investigate how the fracture properties change with the relative density $\overline{\rho}$ (i.e., volume fraction of material comprised in a single unit cell), we fabricated samples at 20 ± 0.60, 26 ± 0.70, and 33 ± 1.4%, and 8 ± 0.44, 12 ± 0.86, and 23 ± 0.61% by tuning the lattice beam radius (D/2, see Fig. 1) in the range 513–689 nm and 645–1126 nm, for the octet and kagome topology, respectively (for more details see Supplementary Section S2.2). For each sample the lattice beam length (L in Fig. 1) was designed to be ∼5 µm. The range of relative densities was restricted by the limits in manufacturing the notch of the CT samples at low volume fractions and the increasing volume of the lattice nodes (Fig. 1), for the octet and kagome topology, respectively.

To explore the whole quasi-static crack growth process, we first performed in-situ tensile fracture experiments on the CT

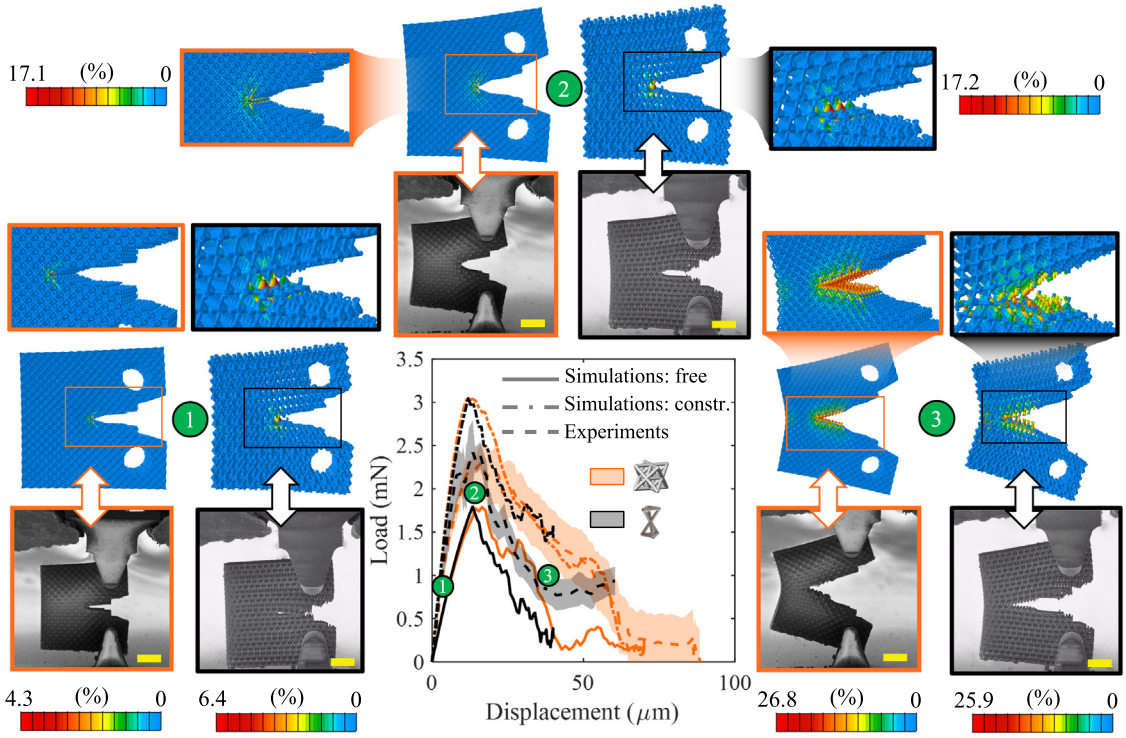

Fig. 2. Stable crack growth in nano-architected lattices. Experimental and numerical load–displacement curves of octet and 3D kagome samples exhibiting three characteristic regions (1, 2, 3). Numerical load–displacement curves are reported for two different boundary conditions at the lower and upper loading pins: free and fully constrained rotations (details in Supplementary Section S5). SEM micrographs and corresponding simulation snapshots evaluated at same (applied) displacement are reported. The equivalent plastic strain contour from simulations highlights the intrinsic plastic toughening mechanism as well as the damaged beams during crack propagation. Scale bar, 25 μm.

samples inside a scanning electron microscope (SEM) (see Methods for details), as shown in Fig. 1, inducing a crack opening mode of loading (i.e., Mode 1). To avoid additional sources of energy dissipation not included in the fracture toughness measurements, the relative rotation between the CT specimen and the loading pins has to be allowed, reducing the friction as much as possible [33]. Fabricating the loading pins and specimen in the same printing process leads to constrained rotations during loading. To overcome this issue, we designed and realized modified pin-to-lattice connections by introducing radial sacrificial supports between the specimen and pins (see Supplementary Section S2.1 and Supplementary Fig. 3) such that they break during vertical displacement of the tension grips.

Three characteristic regions can be identified from the load–displacement curves and SEM micrographs reported in Fig. 2 for both lattice topologies: (1) an initial almost linear mechanical response, (2) a notch blunting configuration at crack initiation, and (3) a softening response region, where stable crack growth occurs (Supplementary Video 2). In the initial region, based on the parent material tensile response (Supplementary Fig. 12) we expected the CT specimen to exhibit elasto-plastic deformations (later confirmed by simulations). Through the different samples and topologies, slightly before reaching the peak load, a first-beam-fracture event (region (2)) occurs (Supplementary Video 2). After that, the crack starts propagating through the specimen orthogonally to the loading direction for both topologies, while the load values gradually decrease (region (3)). From the comparison between the load–displacement curves, and the SEM micrographs of the two topologies (see Fig. 2), two key features emerge. First, the crack trajectory results to be orthogonal to the loading direction for each topology and relative density. We hypothesize that a most-deformed-beam path is followed by the crack during propagation. This assumption is experimentally supported by the observation that fracture seemed to occur at the beams close to the lattice nodes (see Supplementary Fig. 10 and Video 2), thus leading to the breakage of the most deformed beams. Second, the octet samples ($\overline{\rho} \sim 20\%$) seem to dissipate more energy (i.e., area underneath the curve) in region (3) compared to the kagome ones ($\overline{\rho} \sim 20\%$); in addition, the octet architecture exhibits larger displacements at failure (i.e., split of the sample). The SEM micrographs of the octet samples at crack initiation suggest a more pronounced notch blunting effect compared to the kagome ones (region (2) in Fig. 2). This revealed that the octet architecture could be tougher than the 3D kagome one, suggesting the influencing role played by the topology in nano-architected lattices, even over the volume fraction.

To understand the mechanisms and the role of topology on the crack growth, we conducted finite element (FE) simulations (see Methods for more details) on CT specimens as those tested inside the SEM. Due to the extreme computational cost required for simulating stable crack growth in these materials, the geometries were constructed using Timoshenko beam elements. The parent material's response was captured up to complete failure by adopting an elasto-plastic J2 model and a ductile damage model (see Materials and Methods and Supplementary Section S5.1). To validate our experiments and analyses, we first considered two different boundary conditions (BCs) corresponding to free and constrained rotation at the loading pins (see Supplementary Section S5). The experimental load–displacement curves display values in between the numerical results (Fig. 2). The constrained and free rotation BCs can thus be seen as an upper and lower bound, respectively, suggesting that the sacrificial supporting beams (between pins and specimen) partially avoid the influence of friction on the experimental results, and that simulations can provide upper and lower bounds for the measured fracture properties. Accordingly to this, the experimental initial stiffness,

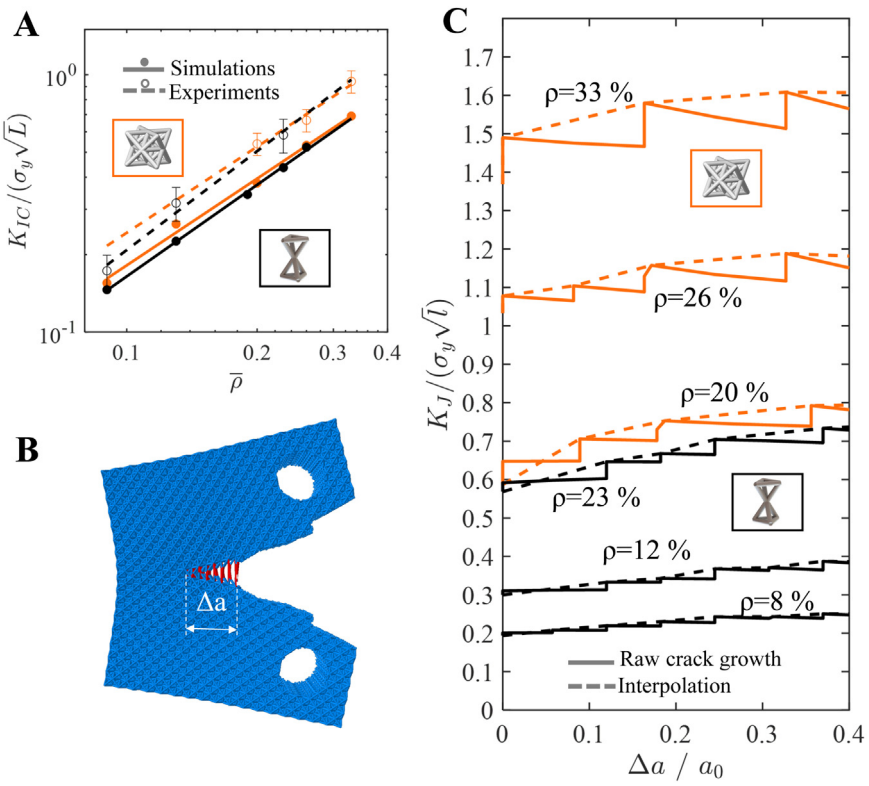

Fig. 3. Fracture initiation toughness and crack growth resistance (i.e., R-curves) of nano-architected lattice materials. (A) Experimental and numerical power-scaling law of normalized fracture toughness (K_J) at crack initiation vs. relative density ($\overline{\rho}$) of octet and kagome lattices. The error bars indicate the maximum deviation from the average value. (B) Representative CT lattice sample with crack extension measure. (C) Numerical R-curves plotted in terms of normalized fracture toughness vs. relative crack length increase ($\Delta a/a_0$) of octet and kagome lattices with experimentally tested relative densities. The solid lines represent the actual simulated curve; the dashed lines represent the interpolation of the peaks. The curves are color coded according to the insets in the plots distinguishing between octet and kagome topology. Free rotation boundary conditions at the loading pins are here considered. (For interpretation of the references to color in this figure legend, the reader is referred to the web version of this article.)

crack initiation load, and dissipated energy during crack growth are bounded by the numerical results, confirming that our simulations can accurately capture the physics of the tests (Fig. 2). Furthermore, the above experimental observations can be confirmed and explained by our model. The orthogonal crack path is perfectly captured by the model (region 3 in Fig. 2) for each relative density and topology (see Supplementary Fig. 14 for the fully constrained condition). The equivalent plastic strain contours plotted in Fig. 2 indicate that the typical hypothesis of small scale yielding does not hold for these nano-architected lattices; intrinsic plastic toughening has thus to be considered. Even in the linear region (1), the beams at the notch tip exhibit plastic flow, with plastic strains comparable for both architectures. Finally, our simulations of the octet specimen predict higher dissipated energy and larger displacements at failure compared to the kagome architecture, as experimentally measured (Fig. 2).

To understand the fracture properties of these materials, we calculated the fracture toughness at crack initiation K_{IC} normalized by the parent material's yield strength σ_y (27 MPa) and the square root of the lattice beam length L (~5 μm), for the octet and kagome topology at different volume fractions $\overline{\rho}$. K_{IC} values were computed by assuming an equivalent-continuum hypothesis, passing through J-integral calculations (details in Supplementary Section S7), as also reported in a recent work [26]. Relying on the numerical model, we further extended the range of relative densities for fracture toughness calculations down to 9 % (9 and 13 % samples were additionally simulated) for the octet topology; we also simulated kagome samples at $\overline{\rho} = 19$ and 26%. As suggested by the measured and simulated peak load, the two topologies tend to have comparable normalized fracture initiation toughness for each relative density (see Fig. 3A). For the sake of clarity, the fracture toughness and R-curves are plotted just for the free BCs. From the double logarithmic regression plot of Fig. 3A a power-scaling law of the form $K_{IC} = \alpha\sqrt{L}\sigma_y\overline{\rho}^{\beta}$ can be deduced, in which α and β represent the scaling and power-exponent coefficient, respectively, generally dependent on the lattice topology and parent material's properties. The experimental and numerical coefficients are reported in Supplementary Table 4. The computationally predicted β for the octet topology matches almost perfectly the experimental value (~1.11), while a relative difference of ~7% is found for the kagome topology. Comparing across topologies, ~14% deviation on the fracture initiation toughness slopes is found (Fig. 3A). The dearth of reports on fracture of nano-architected lattice materials pushed us to compare these results with previous works on macroscopic lattices. As example, the scaling coefficients obtained by Ref. [28] for an ideal titanium octet lattice with rectangular beams' cross-sections were $\alpha = 0.32$, $\beta = 1$. While the power-exponent coefficient (β) of our octet nano-architected lattices is on average ~11% higher, leading to faster performance drop at low relative densities, the scaling coefficient (α) varies between 2.40 and 3.80. This suggests that our octet nano-featured lattices are ~8 times tougher than macroscopic octet titanium structures.

To further understand the influence of the architecture on the fracture properties, we investigated the effects of geometric parameters, such as the lattice beam diameter (D) and length (L), on the fracture initiation toughness. Exploiting the previous experimental and computational data (Fig. 3A), we first deduced an additional power-scaling law relating the fracture toughness and the beams' diameter by $K_{IC} = \tilde{\alpha}\sqrt{L}\sigma_y D^{\tilde{\beta}}$ (see Supplementary

Fig. 19A), where $\tilde{\alpha}$ and $\tilde{\beta}$ have analogous meaning as before. In Supplementary Table 6 the experimental and numerical coefficients are reported for the two topologies (for the free BCs). The power-exponent coefficient, $\tilde{\beta} \sim 2$ for both topologies, reminding the approximated scaling of the relative density with the slenderness ratio (i.e., $\overline{\rho} \propto (D/L)^2$) for slender beams. This suggests that the experimentally observed deviation of ∼10–30% from the linear scaling of the fracture toughness with the relative density ($K_{IC} \propto \overline{\rho}$) (see Supplementary Table 4) might be attributed to different scaling laws of the relative density with lattice beams' geometric parameters. Specifically, fabrication-induced geometric variations in the lattice beams, such as non-constant beam diameter, surface defects, or larger lattice nodes' volume can largely modify such scaling laws [34]. Then, to confirm the fracture initiation toughness scaling with $\sqrt{L}$, we simulated other kagome CT specimens with three different lattice beam length values, 5, 10 and 20 μm, each with relative density 8 and 23%. The range of beams' length and relative density values were chosen to be large enough to allow useful deductions. The results reported in Supplementary Fig. 19B provide power-exponent coefficients of ∼0.5 for both relative densities. Confirming the hypothesis, the fracture initiation toughness of the kagome topology hence approximately scales with $\sqrt{L}$. Analogous considerations would also hold for the octet topology; indeed, existing works have already demonstrated the square-root scaling of K_{IC} with the beams' length [28]. These results overall confirm that the fracture toughness of nano-architected lattice materials scales with the power-law $K_{IC} = \alpha \sqrt{L}\, \sigma_y\, \overline{\rho}^{\beta}$.

Observing no catastrophic failure during in-situ fracture testing and relying on the numerical model, we then obtained from our simulations the crack growth resistance curves (R-curves), which describe the material's resistance to fracture (K_J) as the crack propagates (i.e., crack length increase Δa), as shown in Fig. 3C (see Supplementary Section S7 for more details). First feature to note is that each sample exhibits stair-like shaped R-curves due to the inherent discreteness of lattice materials. Starting for example from the initial notch length ($\Delta a = 0$), the load (thus, K_J) increases as long as every beam on the crack front has not failed. When this occurs, the crack suddenly extends and K_J tends to slightly decrease or remains constant. As observed from the SEM video (Supplementary Video 2), the crack growth in our samples is stable and that is well reflected by the simulated R-curves. Although not pronounced, they display a rising-shape, meaning that the resistance to crack propagation increases and a higher driving force (i.e., external applied stress intensity) is necessary to further crack extension. For example, the normalized K_J after ∼40% of crack growth (i.e., $\Delta a/a_0 = 0.4$) increases of ∼35% for an octet CT sample with $\overline{\rho} = 0.2$ (see Supplementary Fig. 15 for the relative increase of fracture toughness).

Based on these results, it is clear that higher normalized fracture initiation toughness is exhibited by the nano-architected lattices compared to macroscopic titanium lattice structures [28]. In addition, stable crack growth can be reached in nano-architected lattice materials without catastrophic failure. Two different contributions can explain these phenomena. First, the base material's plasticity (see Supplementary Section S5.1), well captured by our numerical model (Supplementary Fig. 12), acts as an intrinsic toughening mechanism locally allowing for large deformations of individual beams (Supplementary Fig. 12), and globally (at the specimen length scale) blunting the crack tip (Fig. 2). Second, it has been shown that materials in general have different behavior at smaller scales [7,8,35]. Specifically, biological [8,36] and man-made nano-architected materials [37] have been demonstrated to exhibit flaw insensitivity (i.e., pre-existing cracks do not propagate; material fails by uniform rupture) when their dimensions approach a critical size. Despite extensive yielding occurs at the base material level, applying linear elastic fracture mechanics to our problem can help to estimate a critical length scale below which the individual lattice beams would allow higher stresses and larger deformations, hence leading to toughening of the nano-architected lattices. Without specific information on the material fracture toughness, harnessing the tensile response of printed IP-Dip micro-pillars in [38] (already used for material calibration, see Supplementary Section S5.1), we first roughly estimated the surface energy, γ, of the base material. We assumed that the dominant flaws are a consequence of the printing process (two-photon lithography). The two main geometric printing parameters are the hatching and the slicing size (see [39] for details); in this case, they were both set to 200 nm (see [38]). The surface energy was determined using the Griffith model:

$$\gamma = \frac{F^2 \pi a \sigma_f^2}{2E}, \tag{1}$$

where F is the adimensional shape factor, dependent on the geometry of the crack and the loading conditions, a is the crack size, E is the Young's modulus, and σ_f is the fracture strength. We considered the experimental values obtained in [38] and during our material model calibration (Supplementary Section S5.1), $E =$ 1.2 to 1.8 GPa, $\sigma_f =$ 78 to 88.3 MPa, and assumed the dominant crack size is between half of and the hatching distance, that is $a =$ 100 to 200 nm. Additionally, to evaluate lower and upper bounds, the shape factor was assumed to be $2/\pi$ to 1.12, corresponding to embedded circular crack and surface crack, respectively [40]. The surface energy was hence found to be in the range 0.21–2.6 J/m^2. From the results in [8,35], the critical size h^* was determined using the following equation:

$$h^* = (1 \div 1.87)\frac{\Gamma E}{\sigma_{th}^2}, \tag{2}$$

where $\Gamma = 2\gamma$ is the fracture energy, and σ_{th} is the theoretical strength, set to $E/30$. The two extreme values of Eq. (2) are obtained by adopting the Griffith and Dugdale–Barenblatt model, respectively; note that the value found in [8] (1.57) falls within this range. Considering the previous range of values, we obtained a critical size for IP-Dip $h^* =$ 215 to 7200 nm. The characteristic lattice beams' diameter (from 1026 to 2252 nm) in the nano-architected lattices we fabricated is consistent with the estimated range of critical size. This indicates that size-effects are possibly responsible for the toughening of the nano-architected lattices. Besides, as experimental evidence, [41] found that IP-Dip printed post-cured nanowires exhibited a pronounced increase of mechanical properties (stiffness, strength and toughness) for a width ∼200–250 nm (tested in the range 200–500 nm), close to our estimated lower bound. Nonetheless, given the large range of possible flaw-tolerant dimensions and the uncertainty on the material fracture toughness, further research is needed to uncover and quantify the contribution of material size effects.

Motivated by the well-known influence of the stress state around a crack on the fracture toughness of materials [40], we exploited the computational model to investigate the role of thickness in nano-architected lattices. We simulated single-unit-cell-thick ($B =$ 7.5 μm and 15 μm for octet and kagome, respectively) CT specimens with same relative densities as the experimentally tested samples ($B =$ 50 μm) (see Supplementary Section S1 for more details on the unit cell definitions). Decreasing the thickness, an average fracture toughness deviation of ∼±5% for the octet and kagome topology, respectively, is exhibited. Therefore, contrary to what expected, thickness (i.e., state of stress) seems not to basically influence the fracture toughness of architected lattice materials with octet and kagome architecture, as shown in Fig. 4A. The comparison between the R-curves in Fig. 4C for two different thickness values brings further

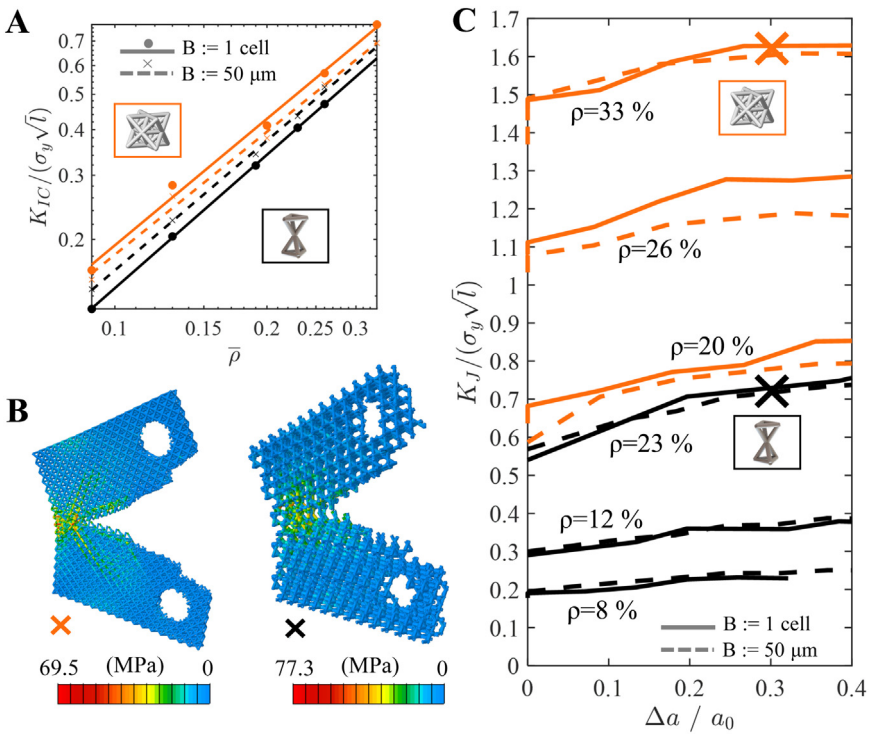

Fig. 4. Role of plane stress/plane strain in architected lattice materials. (A) Effect of thickness on the fracture initiation toughness in the range of relative density 9%–33% and 9%–26% for octet and kagome, respectively, by numerical modeling. One unit cell corresponds to ∼7.5 μm and 15 μm for octet and kagome, respectively (definition of unit cell in Supplementary Section S1). (B) Simulation results of octet (left) and kagome (right) unit-cell-thick specimens (B =1 cell) displaying the crack path and the von Mises stress field at $\Delta a/a_0 = 0.3$. (C) Effect of thickness on the numerical R-curves of octet and kagome lattices at different relative densities. The R-curves are obtained by interpolation of the peaks of the actual stair-like shaped curves.

evidence to the invariance of fracture resistance of through-thickness cracked architected lattices with the stress state. The normalized K_J values during crack propagation of the thinner and thicker samples match closely without significant deviations (on average ∼3%). The crack trajectory in the thin samples follows analogous orthogonal path as in the 50 μm-thick ones, as shown for one relative density in Fig. 4B for both topologies. This corroborates the independence of the results from the specimen's thickness, and consequently from the state of stress around the moving crack tip.

Due to the inevitable presence of imperfections introduced in the architecture during the fabrication process, we wondered whether imperfections may significantly influence the fracture resistance of lattice materials. To answer this question, we exploited our computational model introducing random imperfections into the CT lattice specimens with the goal to resemble realistic printing defects. The imperfections were added displacing each node of the numerical model's mesh along the three spatial directions by a random quantity, constrained to be smaller enough to avoid intersection between adjacent beams and self-intersection (see Supplementary Section S8). The offset of the nodes attempts to resemble the waviness of the lattice beams and the mismatch between the actual and ideal lattice nodes' positions. As expected, imperfections degrade the lattice performance: stiffness and peak load of the CT specimens decrease on average of ∼18%, for the topologies and relative density range analyzed, as shown in Fig. 5A–B. Consequently, the fracture initiation toughness of octet and kagome lattices with imperfections tends to be on average smaller by ∼15 and 21% than that of perfect lattices, respectively. The resulting power-scaling law manifesting a steeper slope β∼1.31 both for octet and kagome topology (see Supplementary Table 5 for a comparison of α and β with and without imperfections) reflects the observed degradation of fracture performance. A small reduction in relative density thus leads to a greater drop in fracture initiation toughness when node-offset imperfections are considered. More evidence of the effect of imperfections is brought by the analysis of the crack growth resistance in Fig. 5D. Imperfections in the octet and kagome lattice lead to an average drop in fracture resistance for the whole simulated crack growth of ∼7 and 18%, respectively, exhibiting some fluctuations due to the stochastic nature of the added defects. It should be noted that the effective Young's modulus (E) of our lattices used for calculating the fracture toughness values (see Supplementary Section S7) changes if imperfections are added. We thus assumed that E degrades likewise the specimen's stiffness (see Supplementary Fig. 16). The crack path is not strongly influenced by the added imperfections, preserving an overall orientation orthogonal to the loading direction, except for slight deviations in the octet topology (Supplementary Fig. 17). Nevertheless, the orthogonality of the crack trajectory is globally preserved. These results suggest that imperfections, together with reducing the global mechanical efficiency (see E reduction), degrade the fracture resistance properties of 3D architected lattice materials, especially at low volume fractions.

3. Conclusions

In summary, through experiments and simulations of 3D nano-architected lattice materials exhibiting stable crack growth, we first uncovered the fracture resistance performance of the octet and 3D kagome architecture. Small differences were found in the fracture toughness at crack initiation and during crack growth (∼3%–8% higher for octet). This suggests that stretching-dominated topologies such as octet, despite being stiffer and stronger than bending-dominated topologies, do not suffer from the trade-off between stiffness, strength and fracture toughness. In addition, the 8-fold normalized fracture toughness increase of the octet nano-featured lattices over macroscopic octet structures suggests that power-scaling laws might change at smaller scales

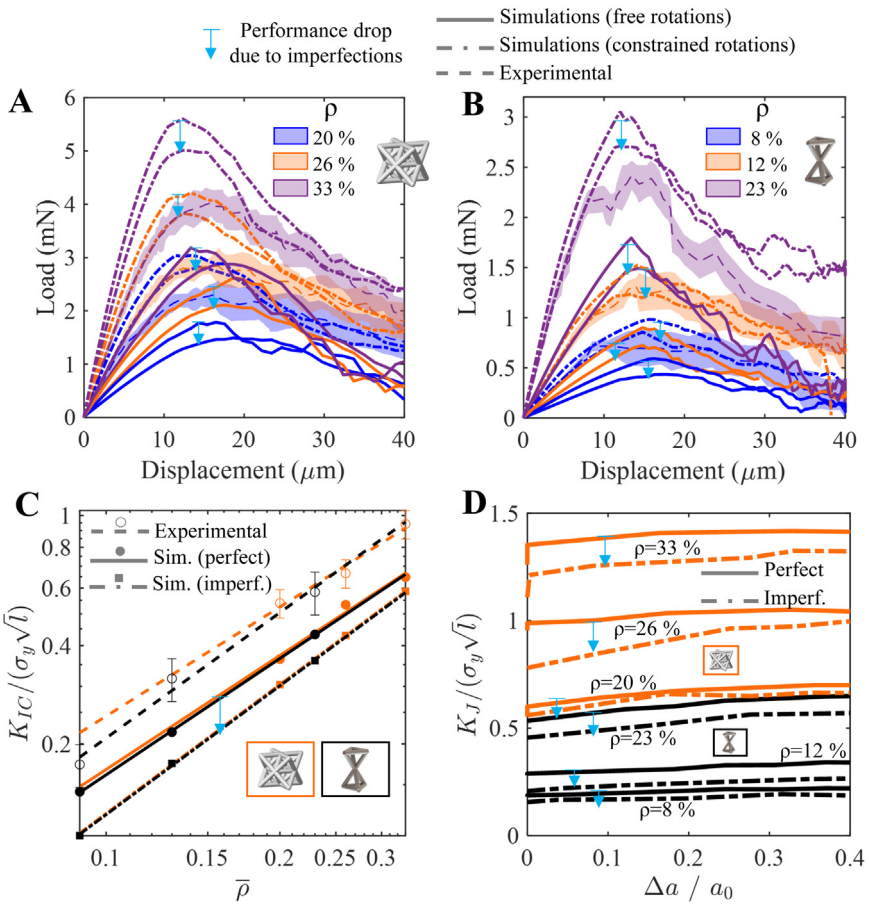

Fig. 5. Role of imperfections on fracture resistance of architected lattice materials. A–B Effect of imperfections on the load–displacement curves, evaluated by comparing numerical simulations of samples with and without imperfections, and experiments for the octet (A), and (B) kagome lattice. Free and constrained boundary conditions at the loading pins are here considered. (C) Effect of imperfections on the normalized fracture initiation toughness power-scaling law. Experimental curves are reported for completeness. The error bars indicate the maximum deviation from the average value. (D) Effect of imperfections on the R-curves. In C and D, for the sake of clarity, only free rotation boundary conditions are displayed. The curves are color coded according to the legends and insets in the plots. The R-curves are obtained by interpolation of the peaks of the actual stair-like shaped curves. (For interpretation of the references to color in this figure legend, the reader is referred to the web version of this article.)

independently of topology, perhaps owing to material size effects. To verify this hypothesis, further comparative studies with same parent material are needed. We want to emphasize that it is not fully clear yet at which scale nano-architecting lattice materials provides superior fracture performance compared to micro- and macro-scaled lattices. Further systematic experimental studies are thus needed to shed light on the size-scaling toughening mechanisms. We then surprisingly discovered how the fracture toughness is overall independent from the samples' thickness, contrary to the plane strain toughness definition in traditional materials. Finally, introducing node offsets in the lattice model's beams, we found that imperfections both degrade mechanical efficiency (i.e., stiffness) and fracture resistance properties (∼7%–18%). Overall, these findings shed light for the first time on the fracture resistance properties of 3D nano-featured lattices. They demonstrate that not only lightweight, stiff and strong materials can be obtained by architecting structures at nano- and micro-scale, but also materials with high normalized fracture toughness can be manufactured.

4. Methods

4.1. Fabrication

Compact tension (CT) samples were designed using CAD SolidWorks software. A Photonic Professional Two-Photon Lithographic instrument (Nanoscribe GmbH) was employed to print the samples in a photoresist polymer resin (IP-Dip) with a slicing of 250 nm, hatching of 200 nm, laser scan speed of 10 mm/s, and laser power of 15 mW. Each sample was written on a Si substrate, which was silanized to improve the adhesion between the sample and the substrate, avoiding delamination during tensile testing. Critical point drying was performed on these samples using Autosamdri 931 (Tousimis). Heating and pressurizing the fluid inside the dryer above the critical point allow to avoid evaporation stresses, that would warp and pre-stress the samples' structure. The samples were then attached to a scanning electron microscope (SEM) stub with colloidal graphite paste, which dries into a stiff adhesion layer between the stub and back of the Si wafer. We assumed this layer being much stiffer than the sample. Finally, the support beams of the samples were removed using a focused gallium ion beam (FIB). To account for the real relative density in the power-scaling law for fracture toughness, we SEM-imaged the printed beams of a selected unit cell in each sample, and reconstructed the actual geometry on SolidWorks. The actual relative density was computed by dividing the model volume by the volume of a solid enclosing the footprint of the cell. Measurements are reported as average values with 95% confidence intervals. Measured values tended to be in average ∼3.4% higher than the designed values; see Supplementary Fig. 6 for all the data.

4.2. In-situ tensile fracture experiments

Quasi-static tensile experiments were performed using a custom-made tension grip attached to a nanoindenter (InSEM, NanomechanicsInc.) installed in an SEM (FEI Quanta 200F) to enable in-situ imaging of the experiments. All lattice samples were loaded at a strain rate of 10^{-3} s^{-1} up to failure. The measured vertical displacements were corrected to account for the compliance of the IP-Dip heads and base (see Supplementary Section S3.1).

4.3. Finite element modeling

To validate the experimental results and obtain R-curves, quasi-static finite element (FE) simulations of the CT samples under tension were performed using the commercial software Abaqus/Explicit (kinetic energy monitored to be below 5% of the internal energy for each simulation). Each strut in the architected lattices was meshed with 7 three-node quadratic 1D Timoshenko beam elements (B32 in Abaqus), found to be an optimal mesh-insensitive value (see Supplementary Section S5.2). Each strut had a circular cross section of radius $D/2$ and length L (for further details see Supplementary Section S1). The IP-Dip parent material's behavior up to failure was captured by adopting an elasto-plastic J2 model with Young's modulus E = 1500 MPa, Poisson's ratio $\nu = 0.4$, power-law hardening of the form $\sigma_y = \sigma_{y0} + H\varepsilon_p^n$ with initial yield stress $\sigma_{y0} = 35$ MPa, hardening coefficient H = 857 MPa, hardening exponent $n = 1.613$, and linear damage evolution with plastic fracture strain $\varepsilon_f = 0.2135$ and plastic displacement at failure $u_f = 0.02$ (see Supplementary Section S5.1). Self-contact and contact between beams was accounted for. To consider only the sample's stiffness (excluding the loading system's stiffness), one dummy node was kinematically coupled with the nodes on the surface of each of the sample's holes. Two displacement boundary conditions (i.e., displacement control) were applied: (1) free rotations, (2) constrained rotations at the loading pins. In (1), the rotations around an out-of-plane axis were allowed, while in (2) were not (see Supplementary Section S5). The procedure for computing the fracture toughness and R-curves is described in Supplementary Section S7.1. To track the crack tip during simulation of crack propagation, an in-house Python script was implemented (Supplementary Section 7.1).

Declaration of competing interest

The authors declare that they have no known competing financial interests or personal relationships that could have appeared to influence the work reported in this paper.

Data availability

Data will be made available on request.

Acknowledgment

JRG gratefully acknowledges the financial support of the Vannevar-Bush Faculty Fellowship from the US Department of Defense.

Appendix A. Supplementary data

Supplementary material related to this article can be found online at https://doi.org/10.1016/j.eml.2022.101883.

References

[1] J. Aizenberg, J.C. Weaver, M.S. Thanawala, V.C. Sundar, D.E. Morse, P. Fratzl, Skeleton of Euplectella sp.: Structural hierarchy from the nanoscale to the macroscale, Science 309 (5732) (2005) 275–278.
[2] K.J. Koester, J. Ager, R. Ritchie, The true toughness of human cortical bone measured with realistically short cracks, Nature Mater. 7 (8) (2008) 672–677.
[3] R. Lakes, Materials with structural hierarchy, Nature 361 (6412) (1993) 511–515.
[4] P. Fratzl, R. Weinkamer, Nature's hierarchical materials, Prog. Mater. Sci. 52 (8) (2007) 1263–1334.
[5] U.G. Wegst, H. Bai, E. Saiz, A.P. Tomsia, R.O. Ritchie, Bioinspired structural materials, Nature Mater. 14 (1) (2015) 23–36.
[6] Y. Jia, H.-L. Wang, B. Liu, Y. Huang, H. Gao, Intrinsic-to-extrinsic transition in fracture toughness through structural design: A lesson from nature, Extreme Mech. Lett. 37 (2020) 100685.
[7] J.R. Greer, W.C. Oliver, W.D. Nix, Size dependence of mechanical properties of gold at the micron scale in the absence of strain gradients, Acta Mater. 53 (6) (2005) 1821–1830.
[8] H. Gao, B. Ji, I.L. Jäger, E. Arzt, P. Fratzl, Materials become insensitive to flaws at nanoscale: lessons from nature, Proc. Natl. Acad. Sci. 100 (10) (2003) 5597–5600.
[9] X. Zhang, Y. Wang, B. Ding, X. Li, Design, fabrication, and mechanics of 3D micro-/nanolattices, Small 16 (15) (2020) 1902842.
[10] J. Singh, A. Upadhyay, S. Sehgal, A review on metallic micro lattice, Mater. Today: Proc. 33 (2020) 1695–1700.
[11] Z. Vangelatos, C. Li, C. Grigoropoulos, K. Komvopoulos, Comparison of the mechanical performance of architected three-dimensional intertwined lattices at the macro/microscale, Extreme Mech. Lett. 40 (2020) 100930.
[12] S.N. Khaderi, M. Scherer, C. Hall, U. Steiner, U. Ramamurty, N. Fleck, V. Deshpande, The indentation response of nickel nano double gyroid lattices, Extreme Mech. Lett. 10 (2017) 15–23.
[13] Z.-H. Jin, A microlattice material with negative or zero thermal expansion, Compos. Commun. 6 (2017) 48–51.
[14] J. Bauer, L.R. Meza, T.A. Schaedler, R. Schwaiger, X. Zheng, L. Valdevit, Nanolattices: an emerging class of mechanical metamaterials, Adv. Mater. 29 (40) (2017) 1701850.
[15] Z. Vangelatos, G.X. Gu, C.P. Grigoropoulos, Architected metamaterials with tailored 3D buckling mechanisms at the microscale, Extreme Mech. Lett. 33 (2019) 100580.
[16] X. Chen, J. Moughames, Q. Ji, J.A.I. Martínez, H. Tan, S. Adrar, N. Laforge, J.-M. Cote, S. Euphrasie, G. Ulliac, et al., Optimal isotropic, reusable truss lattice material with near-zero Poisson's ratio, Extreme Mech. Lett. 41 (2020) 101048.
[17] M. Diamantopoulou, C.C. Roth, T. Tancogne-Dejean, C.M. Lauener, D. Mohr, Ceramic/polymer microlattices: Increasing specific energy absorption through sandwich construction, Extreme Mech. Lett. 53 (2022) 101708.
[18] X. Zheng, H. Lee, T.H. Weisgraber, M. Shusteff, J. DeOtte, E.B. Duoss, J.D. Kuntz, M.M. Biener, Q. Ge, J.A. Jackson, et al., Ultralight, ultrastiff mechanical metamaterials, Science 344 (6190) (2014) 1373–1377.
[19] J. Bauer, A. Schroer, R. Schwaiger, O. Kraft, Approaching theoretical strength in glassy carbon nanolattices, Nature Mater. 15 (4) (2016) 438–443.
[20] C.M. Portela, B.W. Edwards, D. Veysset, Y. Sun, K.A. Nelson, D.M. Kochmann, J.R. Greer, Supersonic impact resilience of nanoarchitected carbon, Nature Mater. (2021) 1–7.
[21] S. Maiti, M. Ashby, L. Gibson, Fracture toughness of brittle cellular solids, Scr. Metall. 18 (3) (1984) 213–217.
[22] N.E. Romijn, N.A. Fleck, The fracture toughness of planar lattices: Imperfection sensitivity, J. Mech. Phys. Solids 55 (12) (2007) 2538–2564.
[23] N.A. Fleck, X. Qiu, The damage tolerance of elastic–brittle, two-dimensional isotropic lattices, J. Mech. Phys. Solids 55 (3) (2007) 562–588.
[24] I. Quintana-Alonso, N.A. Fleck, Fracture of brittle lattice materials: A review, in: Major Accomplishments in Composite Materials and Sandwich Structures, Springer, 2009, pp. 799–816.
[25] H.C. Tankasala, N.A. Fleck, The crack growth resistance of an elastoplastic lattice, Int. J. Solids Struct. 188 (2020) 233–243.
[26] M.-T. Hsieh, V.S. Deshpande, L. Valdevit, A versatile numerical approach for calculating the fracture toughness and R-curves of cellular materials, J. Mech. Phys. Solids 138 (2020) 103925.
[27] R. Manno, W. Gao, I. Benedetti, Engineering the crack path in lattice cellular materials through bio-inspired micro-structural alterations, Extreme Mech. Lett. 26 (2019) 8–17.
[28] M.R. O'Masta, L. Dong, L. St-Pierre, H. Wadley, V.S. Deshpande, The fracture toughness of octet-truss lattices, J. Mech. Phys. Solids 98 (2017) 271–289.
[29] H. Gu, S. Li, M. Pavier, M.M. Attallah, C. Paraskevoulakos, A. Shterenlikht, Fracture of three-dimensional lattices manufactured by selective laser melting, Int. J. Solids Struct. 180 (2019) 147–159.

[30] L. Montemayor, W. Wong, Y.-W. Zhang, J. Greer, Insensitivity to flaws leads to damage tolerance in brittle architected meta-materials, Sci. Rep. 6 (1) (2016) 1–9.
[31] A.J. Mateos, W. Huang, Y.-W. Zhang, J.R. Greer, Discrete-continuum duality of architected materials: failure, flaws, and fracture, Adv. Funct. Mater. 29 (5) (2019) 1806772.
[32] A.J.D. Shaikeea, H. Cui, M. O'Masta, X.R. Zheng, V.S. Deshpande, The toughness of mechanical metamaterials, Nature Mater. 21 (3) (2022) 297–304.
[33] A. International, Standard Test Method for Measurement of Fracture Toughness, ASTM International, 2015.
[34] L.R. Meza, G.P. Phlipot, C.M. Portela, A. Maggi, L.C. Montemayor, A. Comella, D.M. Kochmann, J.R. Greer, Reexamining the mechanical property space of three-dimensional lattice architectures, Acta Mater. 140 (2017) 424–432.
[35] H. Gao, S. Chen, Flaw tolerance in a thin strip under tension, J. Appl. Mech. 72 (2005) 732–737.
[36] B. Ji, H. Gao, Mechanical properties of nanostructure of biological materials, J. Mech. Phys. Solids 52 (9) (2004) 1963–1990.
[37] X. Zhang, A. Vyatskikh, H. Gao, J.R. Greer, X. Li, Lightweight, flaw-tolerant, and ultrastrong nanoarchitected carbon, Proc. Natl. Acad. Sci. 116 (14) (2019) 6665–6672.
[38] W.P. Moestopo, A.J. Mateos, R.M. Fuller, J.R. Greer, C.M. Portela, Pushing and pulling on ropes: hierarchical woven materials, Adv. Sci. 7 (20) (2020) 2001271.
[39] J. Bauer, A. Guell Izard, Y. Zhang, T. Baldacchini, L. Valdevit, Programmable mechanical properties of two-photon polymerized materials: from nanowires to bulk, Adv. Mater. Technol. 4 (9) (2019) 1900146.
[40] N. Dowling, Mechanical Behavior of Materials: Engineering Methods for Deformation, Fracture, and Fatigue, Prentice Hall, 1993, URL: https://books.google.it/books?id=NJNRAAAAMAAJ.
[41] I.S. Ladner, M.A. Cullinan, S.K. Saha, Tensile properties of polymer nanowires fabricated via two-photon lithography, RSC Adv. 9 (49) (2019) 28808–28813.